Available online at www.sciencedirect.com

ScienceDirect

Physics Procedia 10 (2010) 197–203

Physics Procedia

www.elsevier.com/locate/procedia

3rd International Symposium on Shape Memory Materials for Smart Systems

SMA Actuators for Morphing Wings

V. Brailovski*, P. Terriault, T. Georges and D. Coutu

École de Technologie Supérieure, 1100, Notre-Dame Street West, Montreal (Quebec), H3C 1K3 Canada

Abstract

An experimental morphing laminar wing was developed to prove the feasibility of aircraft fuel consumption reduction through enhancement of the laminar flow regime over the wing extrados. The morphing wing prototype designed for subsonic cruise flight conditions (Mach 0.2…0.3; angle of attack -1…+2°), combines three principal subsystems: (1) flexible extrados, (2) rigid intrados and (3) an actuator group located inside the wing box. The morphing capability of the wing relies on controlled deformation of the wing extrados under the action of shape memory alloys (SMA) actuators. A coupled fluid-structure model of the morphing wing was used to evaluate its mechanical and aerodynamic performances in different flight conditions. A 0.5 m chord and 1 m span prototype of the morphing wing was tested in a subsonic wind tunnel. In this work, SMA actuators for morphing wings were modeled using a coupled thermo-mechanical finite element model and they were wind-tunnel validated. If the thermo-mechanical model of SMA actuators presented in this work is coupled with the previously developed structure-aerodynamic model of the morphing wing, it could serve for the optimization of the entire morphing wing system.

Keywords: morphing wing, shape memory alloys, actuators, modeling, finite elements

1. Introduction to the concept of the Morphing Laminar Wing

During the last decade, a significant interest in cleaner aircraft has prompted numerous works on morphing wing structures [1] - [5]. With this perspective, the CRIAQ7.1 “Laminar flow improvement on an aeroelastic research wing” project was initiated three years ago to prove the feasibility of reducing aircraft fuel consumption and greenhouse gas emission through enhancement of the laminar flow regime over an active wing body [6]. Within the framework of this project, an experimental Morphing Laminar Wing (MLW) was designed, manufactured and tested in a subsonic wind tunnel [7] - [10]. The 2D WTEA supercritical airfoil was selected as the reference profile for a morphing laminar wing with a 500 mm chord and a 990.6 mm span. This WTEA airfoil has a maximum thickness/chord ratio of 16% and is similar to a family of natural laminar flow-capable, supercritical airfoils [11]. The morphing wing prototype designed for subsonic cruise flight conditions (Mach 0.2…0.3; angle of attack -1…+2°) combines three principal subsystems: (1) flexible extrados, (2) rigid intrados and (3) an actuator group located inside the wing-box. This paper focuses on the numerical modeling and validation of the SMA actuators that power the morphing wing structure.

The MLW active structure consists of a flexible extrados (skin) and actuators connected together by a transmission system, subjected to variable flow conditions (aerodynamic loads). As presented in Fig. 1a, modification of the airfoil profile occurs when two Shape Memory Alloy (SMA) actuators located inside the wing box apply independently-controlled displacements (δ_1 and δ_2) to the flexible extrados. The overall stiffness and integrity of the experimental wing is provided by the rigid intrados. The force and displacement requirements for each actuator were directly obtained from the finite elements structural analysis for the morphing wing structure for each of the flow cases studied and their maximum and minimum values are displayed in Table 1.

* *Corresponding author. Tel.: (1-514)396-8594; fax: (1-514)396-8530.*
E-mail address: vladimir.brailovski@etsmtl.ca.

1875-3892
doi:10.1016/j.phpro.2010.11.098

Table 1: Requirements for Actuators 1 and 2 (adapted from [8])

Parameters	Actuator 1		Actuator 2	
	min	max	min	max
Vertical extrados displacement, δ (mm)	0	8.16	0	4.1
Actuation force per 1m of span, F_{act} (N)	15	1800	420	1760
Aerodynamic force per 1m of span, F_{aero} (N)	510	1800	410	1420
Extrados stiffness coefficient, k_{ext} (N/mm)	43.8	110.6	-28.6	613.4

2. Design of the SMA actuator group

The actuator group, illustrated schematically in Fig. 1b, consists of four main subsystems: the SMA active element, the transmission system (including the slider and the crank), the flexible extrados and the compression bias spring (for simplicity, only one actuator is shown here). The SMA element is connected to the flexible extrados through the transmission system. The bias spring is placed in parallel with the SMA element. The use of the transmission system allows adjustment of the force-stroke actuator characteristics to the force-displacement characteristics of the flexible extrados.

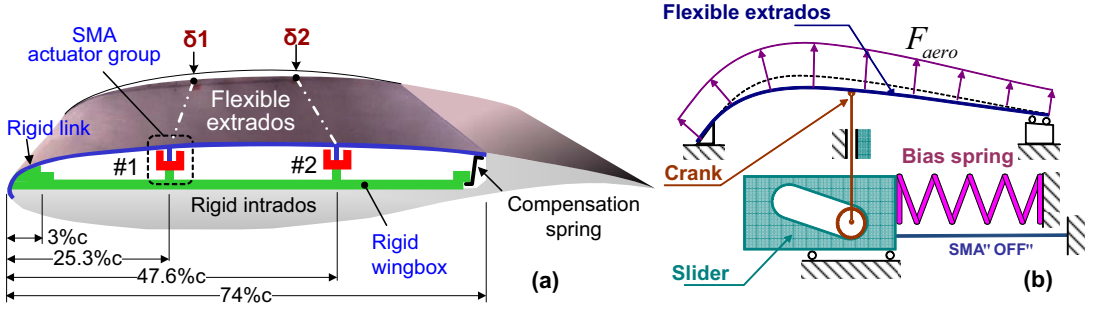

Fig. 1: (a) MLW concept with active extrados (b) SMA actuator's schematic design (from [8] and [9]).

When the SMA actuator is "OFF", the compression bias spring pushes the slider to the left, which corresponds to the nominal extrados position, while the aerodynamic suction forces pull the flexible extrados upward. When the SMA actuator is "ON", it compresses the bias spring and moves the slider to the right, which corresponds to the deployed extrados position. Given the presence of the transmission system with ratio R, the aerodynamic forces and the forces related to the extrados reaction transmitted to the active element and the bias spring, will be decreased by a factor of R, while the stroke provided by the active element will be increased by the same factor R.

The behavior of such an active structure is the result of the interaction between the active SMA element, the bias spring and the flexible extrados, submitted to variable aerodynamic forces. If the flexural extrados stiffness, the pressure distribution and the extrados displacements from the nominal to the target position are known, the design of the active structure can then be completed by selecting an appropriate SMA element and bias spring.

In our case, Actuator 1 should meet higher functional requirements than Actuator 2 (Table 1), and it is thus a critical element of the application. In this work, the use of a compression gas spring as a bias element is privileged because this device applies quasi-constant forces, thus decreasing the power requirements for SMA active elements. The SMA wires are disposed along the span direction and a pulley system is used to double their working length. Based on these premises, it was determined (in [9]) that for the selected transmission ratio of R=3, each actuator should contain six 1.8 m long Ti-50.26at%Ni wires (Special Metals Corp. NY) with a cross-section of 0.7 mm^2 each.

3. Thermo-mechanical modeling of SMA actuators

In the previous sections, the required length (L = 1.8 m) and cross-section (S = 4.2 mm^2) of the SMA active element were determined. This section briefly presents a coupled thermo-mechanical model of an SMA active element and its implementation into the commercial finite element software ANSYS to simulate the temporal response of the SMA wire actuator. The calculations are carried out by using a coupled model containing mechanical and electro-thermal modules. The micromechanical model calculates the evolution of the phase transformation in the wire actuator and the thermal model calculates the temperature of the wire controlled by direct electric heating.

The micromechanical model of an SMA active element, based on the work of Likhachev [12], calculates the strain (ε) corresponding to given wire temperature (T_W) and stress (σ). Since the wire is exclusively loaded in tension, the elongation (δ) and force (F) are directly related to stress and strain (ε = δ /L and σ = F/S). The total strain is the sum of two contributions:

elastic (ε_{el}) and phase transformation (ε_{tr}) strains. Thermal expansion strains are not taken into account because they are considered negligible compared to the other two contributions.

$$\varepsilon = \varepsilon_{el} + \varepsilon_{tr} \tag{1}$$

The elastic contribution is simply given by the elastic properties of austenite and martensite weighted by their respective volume fractions:

$$\varepsilon_{el} = \left[\frac{\Phi_A}{E_A} + \frac{\Phi_M}{E_M} \right] \sigma \tag{2}$$

where E_A and E_M are the Young's moduli of austenite and martensite and Φ_A and Φ_M are the global volume fractions of austenite and martensite respectively, inside the SMA wire. At any time, the two following conditions must be respected:

$$\begin{cases} \Phi_A + \Phi_M = 1 \\ 0 \le \Phi_M \le 1 \end{cases} \tag{3}$$

The calculation of the phase transformation contribution starts by assuming that the SMA wire is divided into N regions connected in series (see Fig. 2a), and that the phase transformation of the i^{th} region is oriented along a single direction defined by the orientation angle θ_i. The amplitude of the phase transformation variation in the region is a product of the maximum intrinsic transformation strain ε_{MAX} and the volume fraction of martensite, ϕ_i.

The parameter ε_{MAX} is the maximum axial strain that can be obtained by the phase transformation in a single crystal, which is identical for each region. The volume fraction of martensite, ϕ_i is the proportion of martensite inside a region with respect to its initial volume, not with respect to the entire volume of the wire, and can therefore be greater than 1. Finally, since each region has its own orientation angle with respect to the wire's longitudinal axis, the transformation strain in each region must be projected on the wire's longitudinal axis and averaged to obtain the global phase transformation strain of the SMA wire:

$$\varepsilon_{tr} = \frac{1}{N} \sum_{i=1}^{N} \phi_i \varepsilon_{max} \cos \theta_i \tag{4}$$

The global volume fraction of martensite is obtained by averaging the volume fractions of all regions:

$$\Phi_M = \frac{1}{N} \sum_{i=1}^{N} \phi_i \tag{5}$$

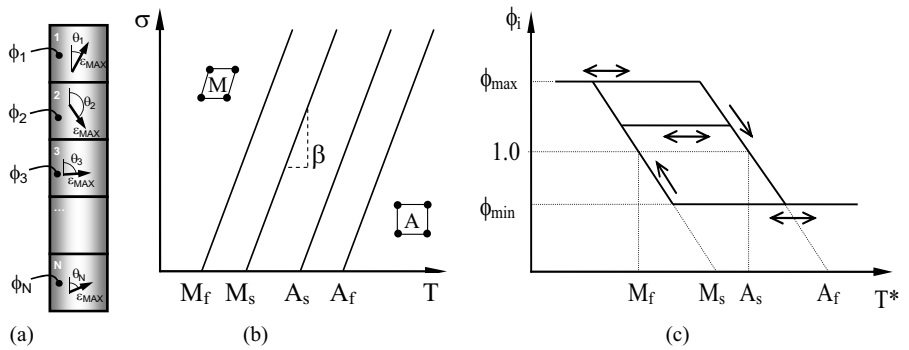

Fig. 2: a) Schematic representation of an SMA wire with N regions, b) state diagram showing the Clausius-Clapeyron coefficient, and c) kinetic rule of the evolution of the volume fraction of martensite in each region.

To find the volume fraction of martensite in each region, the concept of equivalent temperature (T*) is used. This approach considers the fact that the phase transformation, due to its thermo-mechanical nature, can be induced either by stress or by temperature, according to the Clausius-Clapeyron relation.

$$T_i^* = T_W - \frac{\sigma \cos \theta_i}{\beta} \tag{6}$$

where T_i* is the equivalent temperature of the i^{th} region and β is the Clausius-Clapeyron coefficient, which is the slope of characteristic temperatures on the temperature-stress state diagram (Fig. 2b). Four characteristic temperatures M_f, M_s, A_s and A_f represent martensite (M) and Austenite (A) finish and start temperatures. For the same loading given by a wire temperature T_W and stress σ, each region will have a different equivalent temperature T_i* due to its different orientation θ_i. Knowing the equivalent temperature of a region, the corresponding volume fraction of martensite is given by the phase transformation kinetic rule shown in Fig. 2c.

A unit cell of austenite can be transformed into multiple variants of martensite (24 in the case of B2-B19' transformation of Ti-Ni SMA); the phase transformation can have different crystallographic orientations and not necessarily only one, as postulated by equation (4). To compensate this simplification of the model, the volume fraction of martensite in one single region i can reach a maximal value (ϕ_{max}) larger than unity. This means that the more favourable phase transformation orientation in one region can replace the less favourable orientation occurring in the neighbouring regions. Here, it is assumed that ϕ_{max} = N, meaning that the phase transformation in one region can ultimately occupy the entire volume of the model. Finally, a minimum volume fraction of martensite (ϕ_{min}) can be non-zero to simulate some kind of irreversible phase transformation phenomena such as trapped martensite, but these aspects are not considered in this work ($\phi_{min} \equiv 0$).

The thermal model predicts, according to the heat balance equation (7), variations of the SMA wire temperature (ΔT_W) caused by the four following phenomena:

- Joule heating (R: electrical resistance of the wire, i: electrical current and Δt: time increment),
- Exothermic (or endothermic) aspects of the phase transformation (Q_{PT}: latent heat of transformation, S: cross-section and L: length of the specimen; $\Delta\Phi_M$: increment of the martensite volume fraction),
- Convective heat exchanges with the surroundings (h: coefficient of convection, P: perimeter of the wire, T_{AMB}: ambient temperature),
- Specific heat capacity of the material (C_p: specific heat, d: density).

$$\Delta T_W = \frac{i^2 R\Delta t + Q_{PT} SL\Delta\Phi_M - hLP(T_W - T_{AMB})\Delta t}{(hLP\Delta t)/2 + C_p dLS} \tag{7}$$

Both models are coupled in the environment of the finite element analysis software ANSYS 11.0 through a user-defined material law called USERMAT. The main goal of this USERMAT is to calculate the response of a wire SMA actuator caused by an electro-thermomechanical loading where the electrical current, the ambient temperature and the force are controlled for a given period of time. The calculations must rely on an iterative algorithm because, on one hand, the wire temperature increment (ΔT_W) calculated by the thermal model must be supplied to the mechanical model, and on the other hand, the evolution of the phase transformation ($\Delta\Phi_M$) calculated by the mechanical model must be supplied to the thermal model. The finite element model used for the simulation is illustrated in Figure 3a,b. The model is quite simple because only a few 2D spar elements (element type LINK180 of ANSYS) are required. Element A, connecting nodes 1 and 2, represents the flexible extrados made of composite material, Element B, the SMA wire, and Element C, the compression bias spring.

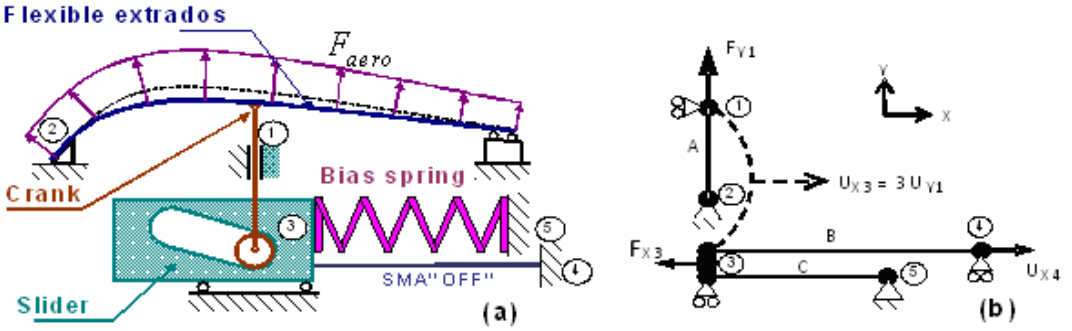

Figure 3: Finite element mesh involving 2D spar elements.

Modeling calibration and set-up

The most demanding case for the actuator is when the aerodynamic force reaches its minimum value while the extrados stiffness coefficient corresponds to its maximum. Therefore, an upward force of F_{Y1} = 510 N is applied at node 1 and a stiffness of 110.6 N/mm is set to element A (see Table 1). Element B connects nodes 3 and 4 and represents the SMA wire actuator. The material constants used for the SMA actuator were experimentally determined and they are collected in Table 2. Node 3 corresponds to the slider that moves horizontally and the connection of the slider to the extrados is numerically achieved by a constraint equation (command CE of ANSYS) where the horizontal displacement of the slider is always three times larger than the vertical displacement of the extrados ($U_{X3} = 3\ U_{Y1}$), given transmission ratio of R=3.

The compression gas spring with a stiffness coefficient of 2 N/mm is represented by Element C which is located between nodes 3 and 5. To keep the extrados in its nominal position when aerodynamic forces reach their maxima, a 1200 N preload is applied to the gas spring [9]. To limit the displacement of the slider in both directions, two compression-only elements, which are extremely stiff and have an initial gap, are added to the model (not shown in Figure 3).

The simulation begins with the SMA wire being stress-free at A_f temperature ($\Phi_M = 0$). The slider is in its nominal extrados position (see Fig. 1b). First, the wire is stress-free cooled down to room temperature. The force F_{X3} is progressively increased up to 1475 N to simulate the installation of the compression bias spring ($F_{X3} = -1200$ N). The SMA actuator is then pre-strained up to 4.4%, which corresponds for the 1.8 m-long SMA wire to a U_{X4} = 79 mm displacement. Finally, aerodynamic loading is simulated by applying a force F_{Y1} = 510 N. The system is now ready to operate.

Note that to guarantee the functional stability of the SMA active element's performances during repetitive recovery strain and stress generations, the following limitations are imposed in the present work: the strain varies between 3 and 5% and the stress varies between 250 and 500 MPa. The application of these constraints is intended to prevent loosening of the SMA wires when the actuator cools down and their overloading and therefore premature degradation when it is heated.

Table 2: Material constants for SMA actuator modeling

Parameter	Symbol	Value	Units
Length	L	1.8	m
Cross-section (6 wires, 0.7 mm^2 each)	S	4.2×10^{-6}	m^2
Perimeter of the wire (6 wires, 3.14 mm each)	P	1.88×10^{-2}	m
Number of regions	N	20	Regions
Martensite start (finish) temperature	$M_s(M_f)$	58 (5)	°C
Austenite start (finish) temperatures	$A_s(A_f)$	30 (85)	°C
Clausius-Clapeyron coefficient	β	7×10^{6}	Pa/°C
Maximum phase transformation strain	ε_{MAX}	0.1045	m/m
Young's modulus of austenite (martensite)	E_A (E_M)	52 (22)	GPa
Resistivity of austenite (martensite)	ρ_A (ρ_M)	$8.2\ (7.6)\times10^{-7}$	Ω.m
Density	d	6450	Kg/m^3
Latent heat of phase transformation	Q_{PT}	100×10^{6}	J/m^3
Specific heat	C_P	320	J/kg/°C
Convection coefficient	h	18	W/m^2/°C

4. Wind-tunnel validation

To validate the proposed design methodology, the wing prototype with two actuators was mounted vertically in the NRC 2 x 3m wind tunnel (Fig. 4a). Two proportional derivative and integral controllers were used to command the actuators using a linear potentiometer (LP804 series, Omega Eng. Inc., CT, USA) for feedback with ±0.15 mm accuracy on the full 8 mm stroke. The force applied by the actuator was measured by the load bolt (SXS-FB-318-24UNF-2.25, Intertechnology, ON, Canada). To control the SMA active elements, two power supplies (SPS 100-33, AMREL Power Product Inc, CA, USA) were used with the displacement signal as a feedback. The data acquisition and the control were performed using LabView software (National Instrument Corp., TX, USA). To stabilize their mechanical properties, the SMA actuators were thermomechanically cycled before their integration in the prototype. The prototype of this morphing wing was tested in the wind tunnel for eight flow cases covering the following flow conditions: Machs 0.2 and 0.3 with angle of attack varying from -1 to 2º, incremented by 1º and showed a drag reduction from 14.5 to 26.7% with an average value of 18.5% under quasi-constant lift conditions Fig. 4b,c).

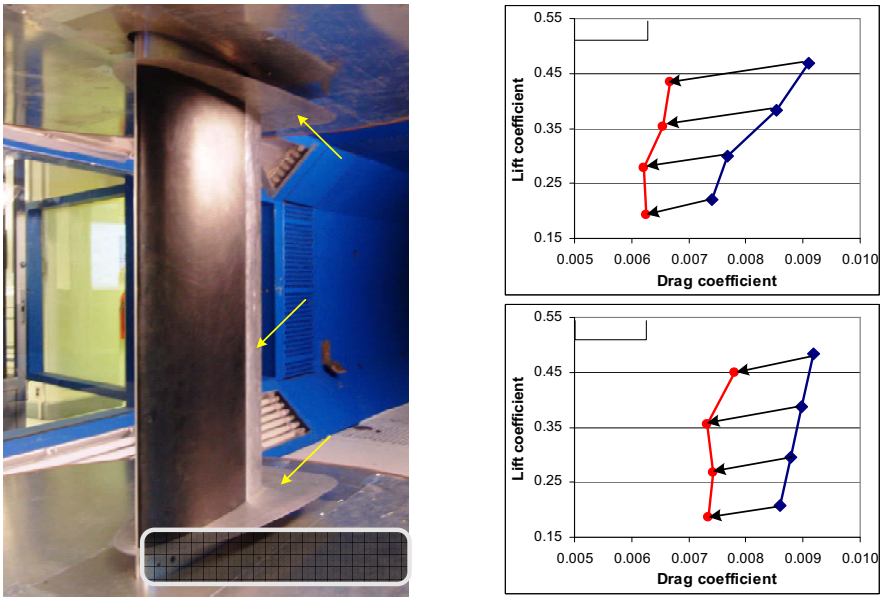

Fig. 4: (a) Experimental morphing laminar wing in the wind tunnel, (b,c) aerodynamic lift versus drag coefficients for flow conditions ranging from alpha -1 to 2º at Machs 0.2 and 0.3 (adapted from [10]).

A real actuation case was simulated, which consisted of morphing the wing extrados from its nominal to the ultimate upward position (8 mm displacement for Actuator 1 and zero displacement for Actuator 2) under the most stringent flow conditions: Mach = 0.2 and angle of attack = -1°. In both cases, electrical current is injected into the SMA element until the deployed extrados position is attained. The current is then cut and the actuator cools down by natural convection to return the extrados to its nominal position. In Fig. 5a, the calculated (dashed lines) and experimental (solid lines) actuator temperature, extrados displacement and electrical energy supplied to Actuator 1 are compared, whereas in Fig. 5b, the calculated and experimental force-stroke trajectories are superposed. Note that to maximize the precision of the actuators' control of the prototype, Pulse Width Modulation (PWM) control approach was used in the wind tunnel. For simulation, on the contrary, the actuation cycle comprised two-step direct current heating: 9.2A for the first 6s and 5.7A over subsequent 88s of heating). Given that thermal energies for both actuation strategies are comparable (see Fig. 5b), the temperature-displacement diagrams obtained numerically and experimentally can indeed be compared. Even though upon heating, the simulation adequately predicts temperature, force and displacement evolutions, it can be observed that mechanical hysteresis caused significant differences between the calculated and the measured force-displacement behaviour of the system upon cooling.

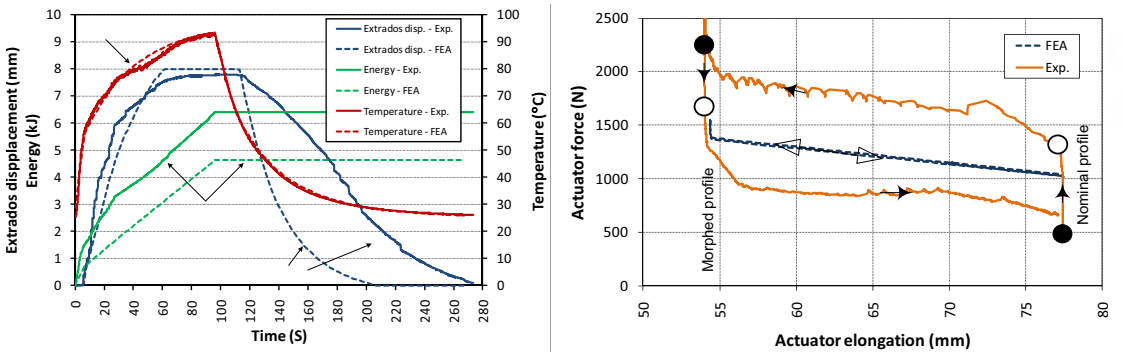

Fig. 5: Actuator 1 - simulated and experimentally measured evolution of the: a) SMA wire temperature, displacement and accumulated heating energy; b) force-elongation: 1-2 (A-B) morphing, 2-1 (B-A) return to the unmorphed profile.

5. Conclusions

In this work, SMA actuators for morphing wings were modeled and then wind-tunnel validated. The coupled thermo-mechanical finite element model resented in this work should be coupled with the previously developed structure-aerodynamic model of the morphing wing to serve for optimization of the entire morphing wing system.

Acknowledgments

The authors would like to thank the Consortium for Research and Innovation in Aerospace in Quebec, the Natural Sciences and Engineering Research Council of Canada, Bombardier Aerospace and Thales Canada for their financial support and acknowledge the contributions of C. Fischer, S. Bérubé and J.-S. Ratelle to the design and manufacture of the experimental morphing wing prototype.

References

[1] The IATA Technology Roadmap Report, 3rd Edition, June 2009.
[2] Boria, F., Stanford B., Bowman S., Ifju, P., AIAA Journal, Vol. 47, No 2 (2009) 399-409.
[3] Strelec J.K., Lagoudas D.C., Khan M.A., Yen J, J. Intell. Mater. Syst. and Struct., Vol. 14, No 4-5 (2003) 257-273.
[4] Hetrick, J.A., Osborn R.F., et al., 48th AIAA/ASME/ASCE/AHS/ASC Conf., (Waikiki, HI, USA, Apr. 23-27 2007), 92-109.
[5] Campanile L. F., Anders, S, Aerosp. Sci. and Technol. J., Vol. 9, No 1, (2005) 55-63.
[6] Brailovski V., Terriault P., Coutu D. et al., ASME Conf. Smart Mat., Adapt. Str. and Intell. Syst., Ellicot City, MA, USA, 2008.
[7] Coutu D., Brailovski V., Terriault P.,J. of Aircraft, Vol. 46, No. 2, (2009) 730-731.
[8] Coutu D., Brailovski V., Terriault P., Aerosp. Sci. and Technol. J., http://dx.doi.org/10.1016/j.ast.2010.01.009.
[9] Georges T., Brailovski V., Morellon E., Coutu D., Terriault P., ASME J. Mech. Design, 131, No. 9, (2009) 091006-1/9.
[10] Coutu D., Brailovski V., Terriault P. et al., Submitted, J. Intell. Mater., Syst. and Struct., April 2010.
[11] Eggleston, B., Poole R.J.D. Jones, D.J.; Khalid, M, J. of Aircraft, vol. 24, No 6 (1987) 405-411.
[12] Likhachev V.A., J. de Phys. IV, Vol. 5, No C8, (1995) 137-142.